Journal of Environmental Management 308 (2022) 114614

Contents lists available at ScienceDirect

Journal of Environmental Management

journal homepage: www.elsevier.com/locate/jenvman

Self-assembling of 3D layered flower architecture of BiOI modified $MgCr_2O_4$ nanosphere for wider spectrum visible-light photocatalytic degradation of rhodamine B and malachite green: Mechanism, pathway, reactive sites and toxicity prediction

S. Balasurya [a], Mohammad K. Okla [b], Asmaa Mohebaldin [c], Abdullah A. AL-ghamdi [b], Mostafa A. Abdel-Maksoud [b], Bander Almunqedhi [b], Hamada AbdElgawad [d], Ajith M. Thomas [e], Lija L. Raju [f], S. Sudheer Khan [a,*]

[a] Nanobiotechnology Laboratory, Department of Biotechnology, Bannari Amman Institute of Technology, Sathyamangalam, Tamil Nadu, India
[b] Botany and Microbiology Department, College of Science, King Saud University, P.O. Box 2455, Riyadh, 11451, Saudi Arabia
[c] College of Medicine, Damascus University, Damascus, Syria
[d] Integrated Molecular Plant Physiology Research, Department of Biology, University of Antwerp, 2020, Antwerpen, Belgium
[e] Department of Botany and Biotechnology, St Xavier's College, Thumba, Thiruvananthapuram, India
[f] Department of Zoology, Mar Ivanios College, Nalanchira, Thiruvananthapuram, India

ARTICLE INFO

Keywords:
$MgCr_2O_4$–BiOI NCs
Photodegradation
Photocatalytic mechanism
Toxicity prediction
Rhodamine B
Malachite green

ABSTRACT

In this study, 3D BiOI nanoparticle (BOI NPs) modified $MgCr_2O_4$ nanoparticle (MCO NPs) was fabricated by simple sonochemical and coprecipitation method for the enhanced photocatalytic activity. The morphological structure of the $MgCr_2O_4$–BiOI nanocomposite (MCO-BOI NCs) was characterized by transmission electron microscopy (TEM), X-ray diffraction (XRD), X-ray photoelectron spectroscopy (XPS), UV–visible diffuse reflectance spectroscopy (DRS), electron impedance spectroscopy (EIS) and photo luminescence (PL). The lower in the PL intensity and small arc in EIS for NCs shows the effective charge separation and lower in rate of recombination of charge carriers in NCs than the pure MCO and BOI NPs. The degradation efficiency of Rhodamine B (RhB) and malachite green (MG) by MCO-BOI NCs was found to be 99.5% and 98.2% receptivity. In addition, the photocatalytic degradation of RhB and MG was studied under various environmental parameters (different pH, varying the concentration of NCs and dyes) and response surface (RSM) plot was performed. The complete mineralization of RhB and MG by MCO-BOI NCs was determined by TOC. In addition, the photocatalytic degradation pathway was elucidated based on GC-MS results and Fukui function. In addition, the toxicity of intermediate formed during the degradation of RhB and MG was predicted by ECOSAR. The present work highlights the application of MCO-BOI NCs in environmental remediation for toxic pollutant removal.

1. Introduction

Major contamination in the water bodies was due to the large discharge of organic pollutants including pharmaceuticals and dyes from industries (Zhang et al., 2019; Liu et al., 2012; Parasuraman et al., 2011). Almost 15% of the environmental pollutant was due to the discharge of organic dye and their effluent discharge to Industrial water system annually (Liu et al., 2012; Parasuraman et al., 2011; Li et al., 2017). Rhodamine B (RhB) is one of the major organic dye pollutants which have been used in the food industry and cosmetic and the higher in the accumulation in human body can leads to cancer (Guo et al., 2011). Due to the higher toxic nature of RhB, its usage was banned, but still it is using in several dye industries (Guo et al., 2011; Wright et al., 2010). In addition, malachite green (MG) is also one of the major organic dye pollutants, which has been widely used in leather, silk and paper industry (Srivastava et al., 2004). MG dye possesses low chemical oxygen demand (COD) equal to zero, which indicates that the pollutant does not undergo biodegradations (Srivastava et al., 2004). The alkaline aqueous medium enables the effective conversion of MG toMGleuco-carbinol, which also causes hazardous effect to living organism (Fischer

* Corresponding author.
E-mail address: sudheerkhan@bitsathy.ac.in (S.S. Khan).

https://doi.org/10.1016/j.jenvman.2022.114614
Received 5 October 2021; Received in revised form 15 January 2022; Accepted 24 January 2022
Available online 1 February 2022

et al., 2011). MG discharge and its contamination in the water bodies can able to causes potential genotoxic, mutagenic, teratogenic and carcinogenic in many animal species, which damages the eco-system (Chen et al., 2010). Several reports show the conversion of MG to leucocarbinol malachite green (LMG) causes the accumulation in fish mucus for 10 days and even longer in fat and organs, which leads to cause cancer (Chen et al., 2010; Culp et al., 2002, 2006; Bergwerff et al., 2003; Mittelstaedt et al., 2004). The higher in the toxic nature of MG, it was banned in USA and EU but still it is used fishery disinfection because of cost effective and high efficiency (Culp et al., 2006). Hence, the complete mineralization of organic pollutant is urgently needs for the environmental water treatment. The available literature shows that several techniques employed for the removal or complete degradation of organic pollutant such as adsorption, chemical coagulation separation, and photocatalysis (Wang et al., 2010; Bessekhouad et al., 2004; Chen et al., 2007; Malato et al., 2009; Natarajan et al., 2011; Ochiai et al., 2012). Semiconductor nanomaterial-based material can be used for the complete mineralization due to enhanced optical, sensing and catalytic activity (Al-Qahtani et al., 2022; Balasurya et al., 2021a, 2021b, 2022). Few researches made efforts on the development of semiconductor based photocatalyst like ZnO, WO_3, V_2O_5 and other metal oxide nanocatalyst for the generation of hydrogen under visible light. Mainly, WO_3Nanoparticles (NPs) was non-toxic and it has wide application due to their optical, electrical and magnetic properties, which is cost effective for the production and it is chemically stable (Lin et al., 2015; He et al., 2016; Wang et al., 2015; Rajamohan et al., 2017; Szilágyi et al., 2012; Martinho et al., 2001).

Semiconductor based photocatalyst such as spinel oxide (AB_2O_4), chromated (XCr_2O_4 = Co, Mn and Zn), ferrites and several metal oxides have widely used in several applications such as sensor element, catalytic support, magnetic material, high temperature ceramic, combustion catalysts and photocatalyst (Kim et al., 1992, 2001; Drazic et al., 1989; Pingale et al., 1996; Finocchio et al., 1995; Abbasi et al., 2019). Chromate based photocatalyst possess extensive activity due to their high surface area with suitable morphology. $MgCr_2O_4$ nanomaterial have widely used in the photocatalytic activity for environmental water treatment due to their extensive property such as higher in thermal stability, melting point and mechanical strength, which can elevate temperatures and humidity-sensing properties (Nayak et al., 2002). Abbasi et al., (2019) synthesized $MgCr_2O_4$ and $MgCr_2O_4$/Ag nanostructures and studied the photocatalytic activity of the nanomaterial against RhB, methyl orange (MO) and methylene blue (MB). They found that the photocatalytic degradation was more effective by $MgCr_2O_4$/Ag NCs than $MgCr_2O_4$ NPs under visible light irradiation (400 W tungsten lamp). According to the previous literature, the narrow band gap energy of MCO was found to be in the range of 1.5–1.9 eV (Finocchio et al., 1996; Andrade et al., 2006; Abbasi et al., 2017). Recently, bismuth oxyhalide (BiOX, X = F, Cl, Br, I) based nanomaterial has been widely used as photocatalyst for the environmental remediation which attracted great attention (Di et al., 2017, 2018, 2019, 2020). Several researchers studied that photocatalytic activity is mainly due to its unique and novel optical, anisotropic layered structure, mechanical and electrical properties (Zhang et al., 2018; Pirhashemi et al., 2018), which restively possess band gap in the range of 1.9–2.7 eV (Pirhashemi et al., 2018; Raza et al., 2021). The relative band gap of BiOI possesses the visible light activation for the optimistic degradation of organic dye pollutant removal (Raza et al., 2021). Here, the pure BiOI sustains lower in the separation and transfer of charge carrier, higher in the rate of recombination of the charge carriers (Raza et al., 2021), which hampered in the photocatalytic application of the pure nanomaterial (Wen et al., 2017). According to the available literature, BiOI possess high vacancy oxygen and it shows excellent photocatalytic activity on removal various environmental pollutant (Zhang et al., 2018; Pirhashemi et al., 2018; Raza et al., 2021; Raza et al., 2021, 2021). As it possesses high oxygen vacancy it can be used for the treatment of various environmental pollutants (Raza et al., 2021). In order to solve the issues, p-type BiOI was decorated on n-type MCO for the relative higher photocatalytic activity. Here, 3D BiOI modified MCO NCs was developed for the complete mineralization of organic pollutant such as RhB and MG, which can be used for the treatment of environmental water pollution.

2. Experiments

2.1. Fabrication of nanomaterial

2.1.1. Preparation of $MgCr_2O_4$

The MCO NPs was fabricated by co-precipitation method and we have adopted Akhundi et al. (2017) method with a slight modification. Briefly, 0.1 M of $MgSO_4$ and 0.1 M of $CrNO_3$ were dissolved in 100 mL distilled H_2O and the suspension was stirred for 120 min. Then, 5 M of NaOH was added dropwise to the reaction mixture until the suspension was reach to pH 10. Afterwards, the reaction mixture was transferred to 250 mL round bottom flask and the reaction mixture was refluxed at 96 °C for 3 h. The appearance of green precipitate indicates the formation of MCO NPs. the particle was collected by centrifugation and washed twice with water and ethanol. The collected particle was dried at 80 °C for 2 h and the collected nanomaterial was calcinated at 520 °C for 4 h.

2.1.2. Preparation of $MgCr_2O_4$–BiOI

The MOC-BOI NCs was fabricated by sonochemcial method. Briefly, 10 mmol of fabricated MCO NPs was sonicated for 40 min under colling jacket to maintain the temperature at 10 °C and labeled as solution A. Then, $BiNO_3$ (1, 2 and 3 mmol) dissolved in 1 mol of HNO_3 was added separately and the suspension was stirred until the clear solution appear and labeled as solution B. Then, the reaction mixture solution B was added dropwise to solution A and stirred for 30 min. Then, 3 mM of KI was added dropwise to the suspension and the reaction mixture was stirred at 80 °C for 30 min. The prepared particles were collected by centrifugation at 10,000 rpm for 10 min and washed twice with water and ethanol. Similarly, pure BOI was fabricated in absence of MCO NPs. The fabricated nanomaterial was named as MCO-BOI-10% ($MgCr_2O_4$–BiOI-10%), MCO-BOI-20% (gCr_2O_4–BiOI-20%) and MCO-BOI-30% ($MgCr_2O_4$–BiOI-30%), MCO ($MgCr_2O_4$) and BOI (BiOI). The detailed description of the morphological and other characterization analysis of fabricated nanomaterial is provided in the Supplementary material Text S1.

2.2. Photodegradation experiments

The photodegradation experiment was performed at 20 mg/L of fabricated photocatalyst (BOI, MCO and MCO-BOI) to the targeted pollutant such as RhB (in presence of 1 mL H_2O_2) and MG, where C_0 = 20 mg/L. Then, the reaction mixture was kept in shaker for 30 min under dark condition to obtain the absorption equilibrium. Thereafter, the reaction mixture was irradiated under visible light (halogen lamp 1000 W). At specific time intervals 2 mL of the reaction mixture was collected and the UV–visible absorption spectra were recorded in the range of 400–700 nm. In addition, the photodegradation of MCO-BOI NCs was studied at various pH parameters (pH 5 to 9). Further, the effect different NCs concentrations (5–25 mg/L) and different concentration of dyes (5–25 mg/L) on photodegradation also recorded. The reusability of the nanomaterial was determined by performing the six-cycle test and the stability of the NCs was determined by XRD and XPS after irradiation. Radical scavenging test was performed by addition of Ethylenediaminetetraacetic acid (EDTA - 1 mL, C = 1 mmol), $AgNO_3$ (1 mL, C = 1 mmol), isopropyl alcohol (IPA – 1 mL) and Benzoquinone (BQ - 1 mL). They were added to the reaction mixture separately in the experiment and the UV–visible absorption spectra were recorded.

2.3. RSM

The experimental design of response surface methodology (RSM) was performed to study the influence of dye concentration, nanoparticle concentration and pH with the response on the degradation efficiency of RhB and MG. The central composite design on the photocatalytic degradation of RhB and MG was performed with three parameters with factorial point (2^4). The surface plot and histogram plot against dye concentration verses NCs concentration, dye concentration verses pH and NCs concentration verses pH was performed to determine the effective degradation of RhB and MG by MCO-BOI NCs.

2.4. Computational analysis

The density function theorem (DFT) analysis was performed for RhB and MG dye. The Fukui function was calculated by Dmol3 by optimized GGA parameter. DFT was performed to determine the HUMO, LUMO and electronic density of RhB and MG dye. Thus, the results predict the radical, electrophilic and nucleophilic attack. The toxicity of intermediates was predicted by ECOSAR software, which provides the data of acute and chronic toxicity on fish, algae and daphnia (Wang et al., 2020a,b).

3. Results and discussion

3.1. Characterization

3.1.1. TEM and SEM

The morphological characteristics of the synthesized MCO, BOI and MCO-BOI NCs were determined by transmission electron microscopy (TEM) and scanning electron microscopy (SEM) analysis (Fig. 1). SEM image of the MCO NPs illustrate that the particle is spherical in shape and the SEM imaging of BOI illustrate the formation 3D nanosheets cluster to form nanoflower (Fig. 1a). SEM elemental mapping of MCO-BOI NCs further confirms the presence of Mg, Cr, O, Bi and I (Fig. 1b). TEM image of MCO-BOI indicates the formation of both flower and spheres (Fig. 1c). In Fig. 1c, the low magnification TEM image indicates the faces of the 3D nanoflower and nanosphere. In the other hand, co-facet with two coexist lattice spacings at 3.14 nm indicate the formation of BOI with hkl plane of (102) and 3.42 nm nm indicate the formation of MCO with corresponding hkl plane of (220) (Fig. 1c2). The formation of two lattice crystal structure confirms the formation of nano-heterojunction of MCO-BOI. Further the crystalline structure of the NCs was determined by the selected area electron diffraction (SAED) pattern. Insert of Fig. 1c1, indicate the crystalline structure formation. Energy dispersive X-ray analysis (EDAX) shows the presence of Mg, Cr,

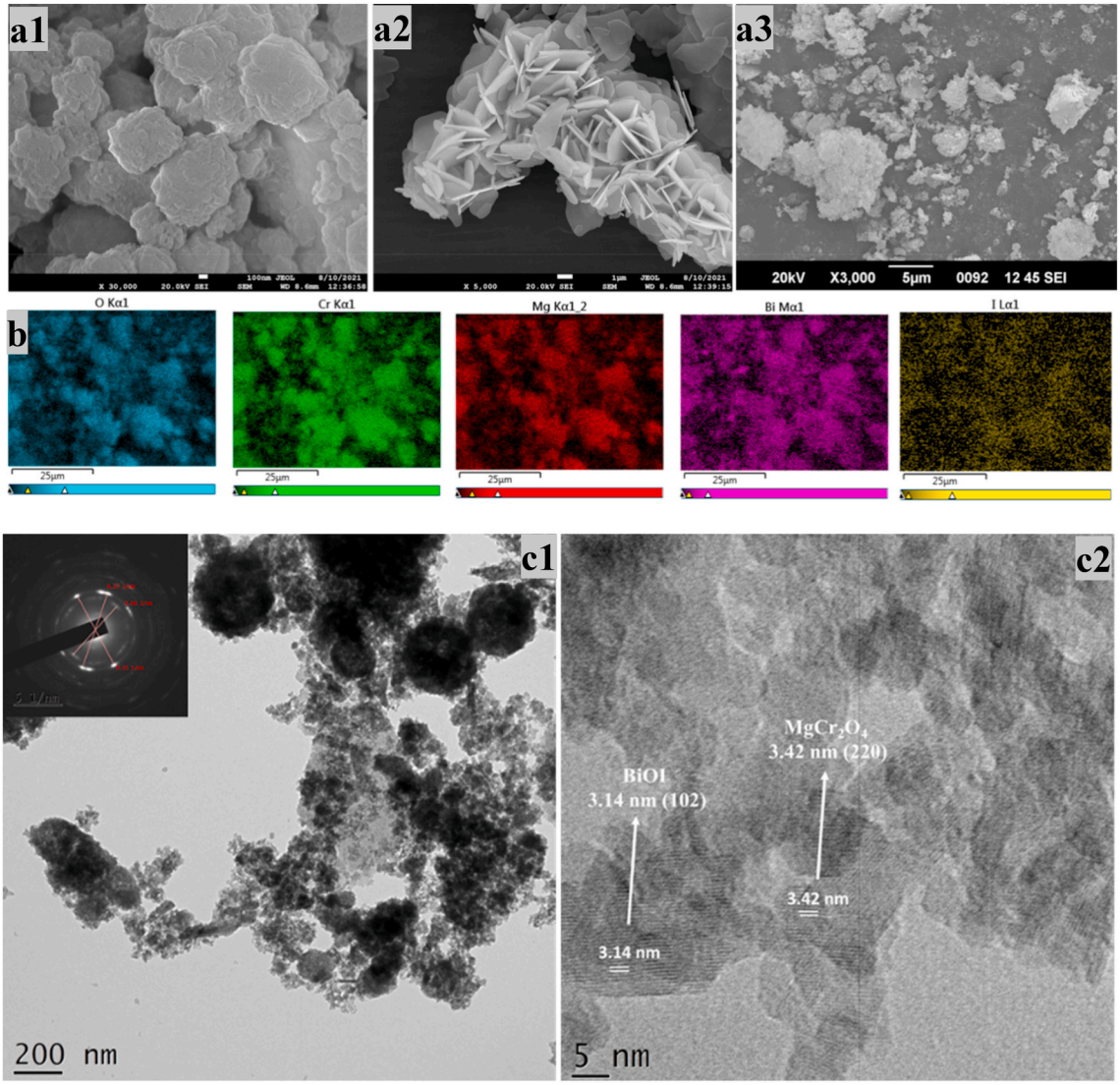

Fig. 1. SEM image of (a1) $MgCr_2O_4$, (a2) BiOI, (a3) $MgCr_2O_4$–BiOI, (b) elemental mapping of $MgCr_2O_4$–BiOI and (c) TEM image of $MgCr_2O_4$–BiOI.

O, Bi, O and I. Further, the weight percentage ratio of Bi, Mg, Cr, I and O was observed to be 16.5%, 14.46%, 32.46%, 35.49% and 1% respectively (Supplementary material Fig. S1a).

3.1.2. XRD

The XRD crystalline pattern of MCO, BOI and MCO-BOI are displayed in Fig. 2a. The XRD pattern of MCO showed sharp peaks at 2θ of 18.8, 35.8, 43.8 and 63.3 with corresponding hkl planes of (111), (311), (440) and (440) (JCPDS card no: 00-010-0351). Further, the XRD pattern of BOI showed sharp peaks at 2θ of 27.5, 31.2, 44.8, 45.9, 53.3, 54.9 and 56.72 with corresponding hkl plane of (101), (110), (103), (200), (104), (114), (212) and (213) (JCPDS card no: 00-010-0351). Thus, the XRD pattern confirms the formation of pure MCO and BOI. In addition, the XRD pattern of MCO-BOI indicate the crystalline phase of both MCO and BOI and thus the result conclude the effective formation of nano heterojunction.

3.1.3. FTIR

The functional group present in MCO-BOI NCs was determined by FTIR analysis and it is displayed in Fig. 2b. The peak stretching at 3570 cm^{-1} corresponds to OH group stretching present in the nanomaterials (Li et al., 2017). The FTIR peak stretching at 1630, 1385 and 1122.58

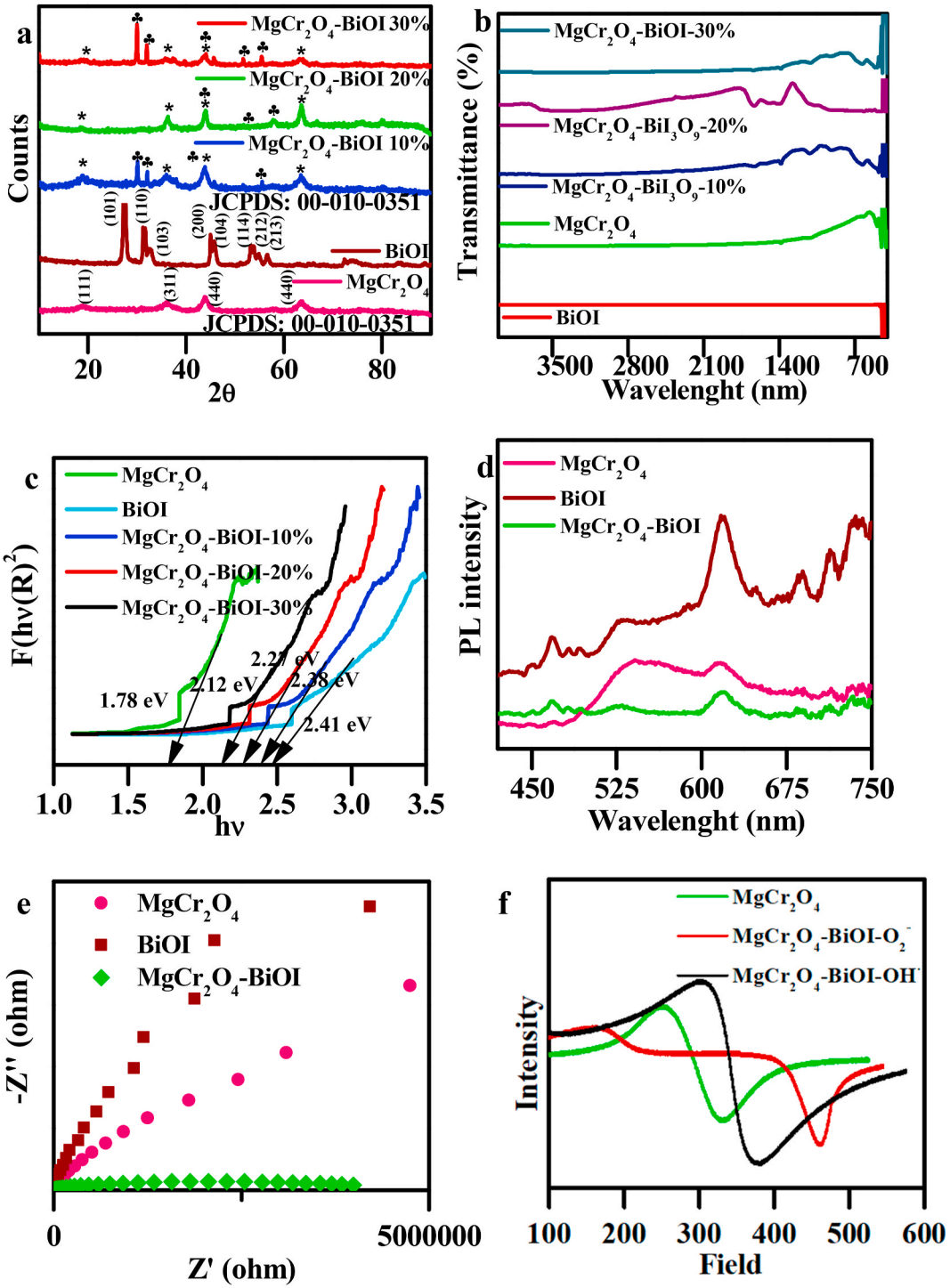

Fig. 2. (a) XRD, (b) FTIR, (c) UV–visible DRS, (d) PL, (e) EIS and (f) ESR of $MgCr_2O_4$, BiOI and $MgCr_2O_4$–BiOI NCs.

cm^{-1} corresponds to the Cr–O and I–O respectively (Finocchio et al., 1995). The peak stretching in the range of 600 to 400 cm^{-1}indicates the metal oxide frame work (Li et al., 2017).

3.1.4. UV–visible DRS

UV–visible diffuse reflectance spectra (DRS) of MCO, BOI and MCO-BOI were analyzed to determine the band gap energy of the nanomaterial. The Kubalka Munk plot was used to determine the band gap energy of the nanomaterial and it is calculated as follow:

$$F(R)hv^2 = A(hv - E_g) \quad (1)$$

where A, ν, h, F, and Eg, were a constant light, frequency, Planck's constant, Kubelka-Munk function and band gap energy respectively. The band gap energy of the pure MCO and pure BOI was calculated to be 1.78 and 2.41 eV (Fig. 2c). Here, the modification of pure MCO by BOI causes the increase in the band gap energy of the composite which causes the red shift (Wen et al., 2017). Thus, the results show the change in the narrow band gap of MCO to visible range leads to effective photocatalytic activity of NCs. The band gap energy shifted from 1.78eV to 2.12 eV, 2.23 eV and 2.38 eV which corresponds to MCO-BOI-10, MCO-BOI-20 and MCO-BOI-30 (Fig. 2c). The shift in the band gap causes the effective charge transfer of the h^+ and e^- separation under visible light irradiation.

3.1.5. Photoluminescence

The charge separation of the fabricated nanomaterial was further determined by photoluminescence analysis. Fig. 2d shows the emission peaks at 615 and 530 nm for MCO and BOI NPs and the observed peaks correspond to the existed vacancies of chromate and bismuthate of near-band edge emission. The emission peak was due to the possible structural defects on various oxidation states of Cr and Bi. The defect structure causes the electrical balance due to the insertion of the lattice O_2^- from environmental O_2 or the occurrence of oxygen vacancies (Xia et al., 2021). Here, after the modification of MCO and BOI causes the lower in the PL intensity of the NCs, which was due to the occupation of the lattice vacancies of both the nanomaterial. The lower in the PL intensity results in the lower in the rate of recombination of h^+ and e^-. Thus, the results show that the enhanced photocatalytic activity of MCO-BOI NCs than pure MCO and BOI NPs.

3.1.6. EIS

The electrochemical impedance spectroscopy (EIS) was further analyzed to determine the charge transport and separation of charge carriers in the nanomaterial (Fig. 2e). The EIS spectra show higher in the frequency of pure MCO and pure BOI than MCO-BOI NCs. The higher in the frequency of impedance spectra shows the higher in the recombination rate in the nanomaterial (Xia et al., 2021). The lower in the impedance spectra of MCO-BOI NCs shows effective charge separation and charge transfer than pure MCO and BOI. Thus, the results also conclude the effective photocatalytic activity of MCO-BOI NCs than pure MCO and BOI NPs.

3.1.7. BET surface area analysis

The surface area of the particle plays a major role in the degradation of organic pollutant. Higher in the surface area of nanocatalyst can interact and adsorb the dye effectively for the effective removal. The BET surface area method was used by several researchers to determine the surface area of the nanocatalyst. The BET plot of adsorption and desorption isotherm of MCO, BOI and MCO-BOI NCs are shown in Supplementary material Fig. S2. Here, the N_2 adsorption and desorption illustrate that the nanocatalyst follows Type – IV isotherm with H3 hysteresis loop structure, which indicated that the fabricated nanomaterial possess mesoporous structure (Phan et al., 2018). The surface area of MCO-BOI NCs (8.74 m^2/g) was higher than the pure MCO and BOI NPs (Table 1). The corresponding pore size (diameter) and pore volume of MCO-BOI NCs was found to be 4.7 nm and 0.010 cm^3/g respectively. The higher in the surface area of the MCO-BOI NCs offers higher interaction with dyes which enhanced the photocatalytic degradation process compared to individual particles.

Table 1
BET surface area, pore volume and pore size values of the prepared nanomaterials.

Sample	Specific surface area (m^2/g)	Average pore diameter (nm)	Pore volume (cm^3/g)
$MgCr_2O_4$	5.05	4.13	0.005
BiOI	4.85	3.48	0.004
$MgCr_2O_4$–BiOI	8.74	4.77	0.010

3.1.8. ESR

The ESR spectra of MCO and MCO-BOI NCs are shown in Fig. 2f. The reactive species involving in photocatalytic degradation process were identified further by using ESR (electron spin resonance) analysis. The spectra represent a broad resonance peak which can be considered due to overlapping of signals that aren't to be separated with confidence as its too close. The signal intensity of MCO-BOI for trapping hydroxyl radical (•OH) is stronger than MCO and BOI. The results also suggest that the amount of holes present in the system of MCO-BOI NCs is higher than that of MCO and BOI.

3.1.9. XPS

The XPS analysis of MCO-BOI NCs was determined which is used to determine the chemical state and surface composition of the materials (Fig. 3). The presence of Mg, Cr, Bi, I and O were confirmed in the XPS analysis. The presence of O was confirmed by sharp peak at 528.5 eV with corresponding orbital spin of 1S. The XPS spectra of O 1S showed the fitting peak at 528.5 and 538.3 eV which corresponds to the metal oxygen and surface oxygen adsorbed to the nanomaterial (Finocchio et al., 1996; Zhang et al., 2018). The XPS spectra of Bi showed strong peak at 157.6 and 163.1 eV which corresponds to the orbital spin of $4f_{7/2}$ and $4f_{5/2}$ respectively (Zhang et al., 2018). The sharp peaks at 575.3 584.6 eV corresponds to Cr $2p_{3/2}$ and $2p_{½}$ ((Finocchio et al., 1996). XPS spectra of I showed sharp peaks at 617.8 and 634.8 eV which corresponds to the spin orbital of $3d_{5/2}$ and $3d_{3/2}$. The peaks at 662.6 and 634.6 eV were due to the satellite peak of I (Zhang et al., 2018). The sharp peak at 1303.2 eV corresponds to Mg with its corresponding spin of 2p (Finocchio et al., 1996). The XPS spectra of MCO-BOI NCs showed both MCO and BOI peaks, which indicates the effective formation of nano heterojunctions.

4. Photocatalytic degradation of RhB and MG

The photocatalytic efficiency of MCO-BIO NCs was evaluated by the photocatalytic degradation of RhB and MG under visible light. The degradation efficiency of MCO-BOI NCs was studied as 10%, 20% and 30% (mol ratio) decoration of BOI on the surface of MCO. The results indicate that 30% decoration of BIO on MCO showed effective degradation of RhB and MG. Here, Fig. 4 a1 and b1 illustrate the UV–visible absorption spectra of the photocatalytic degradation of RhB and MG. The loss in the characteristic peak intensity at 556 nm for RhB and 626 nm for MG observed under visible light irradiation. The complete disappearance of the peak intensity of RhB and MG was found to be 40 and 80 min by MCO-BOI NCs respectively (Fig. 4a1 and b1). The degradation efficiency of NCs on RhB and MG was calculated to be 99.5 and 98.2% respectively (Fig. 4a2 and b2). In addition, the efficiency of the photocatalytic activity of pure MCO and BIO were determined to be 93% and 53% on RhB and 9.8 and 51% on MG respectively. Thus, the results conclude that the degradation efficiency was higher in MCO-BIO NCs than pure MCO and BIO NPs (Fig. 4a and b). From the results it was understood that the formation of heterojunction shows effective

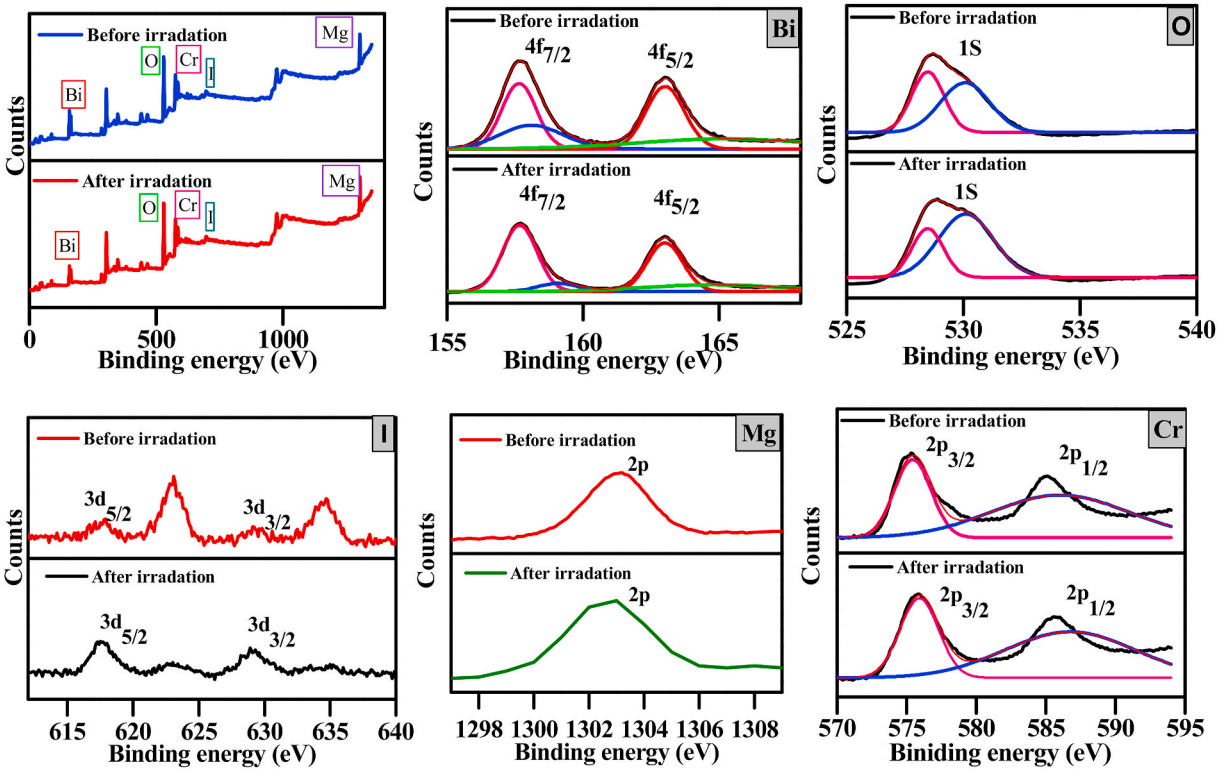

Fig. 3. XPS of $MgCr_2O_4$–BiOI NCs.

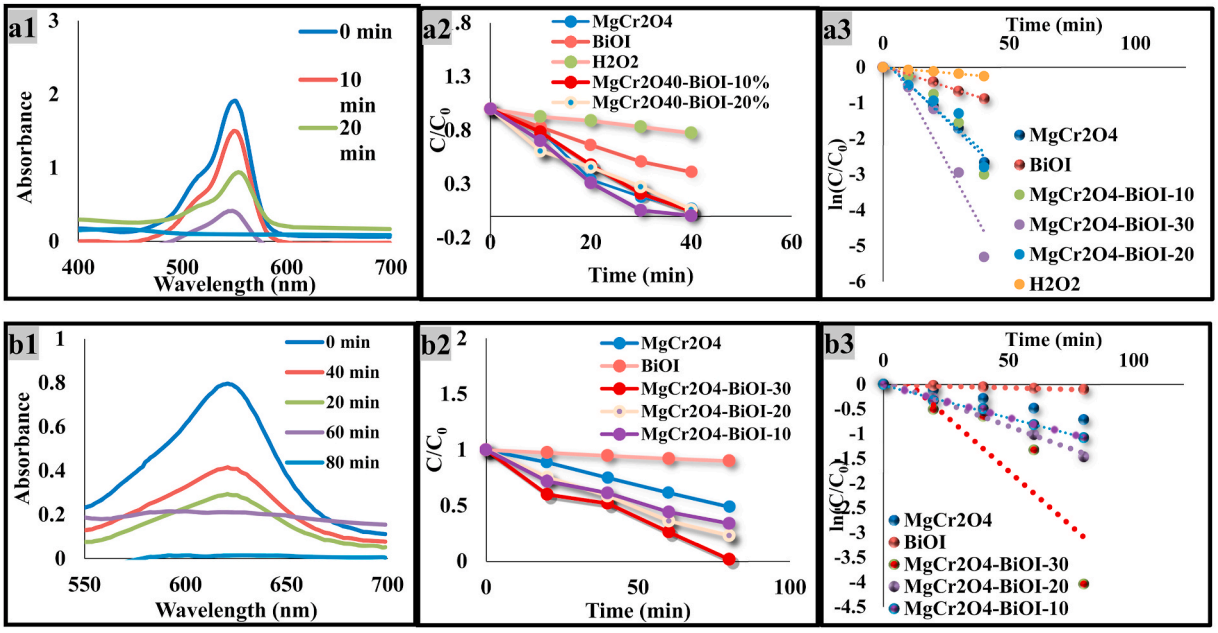

Fig. 4. UV–visible absorption spectra, C/C_0 and $\ln(C/C_0)$ plot on the degradation of (a1, a2 and a3) RhB and (b1, b2 and b3) MG.

degradation under visible light and the rate kinetic and order of the reaction was evaluated by Equ. 2.

$$ln\left(\frac{ct}{co}\right) = kt \ln\left(\frac{ct}{co}\right) = kt \quad (2)$$

Here, C_0 is the absorbance of the solution at time t = 0 and C_t is the absorbance at time 't'. Here, the rate constant for the photocatalytic degradation of RhB and MG by MCO-BIO NCs was found to be 0.025 and 0.0092 min^{-1} which was higher than pure MCO and BIO NPs. In addition, the experimental profile observed in the photodegradation kinetics, and considering that the active sites have a constant number. The increase in the surface area of the NCs shows the effective adsorption of RhB and MG than the pure MCO and BOI NPs. In addition, the regression co-efficient on the photocatalytic degradation of RhB and MG was >0.95 and the reaction is expected to follow first-order kinetics. Table 2 illustrate the comparison of photodegradation of the present work with the available literature. According to the previous literature the effective degradation of RhB and MG achieved was in 70–94% and

Table 2
Comparision of previous work on the degradation of RhB and MG with the present work.

Particle	Dye	Degradation efficiency (%)	Author
CdS QDs/npg-C_3N_4	RhB	71.1	Fan et al. (2016)
Ag_3PO_4	RhB	77.5	Wang et al. (2014)
rGO/$SrTi_{0.95}Fe_{0.05}O_{3-\delta}$	RhB	90	Dong et al. (2017)
BiOCl and BiOBr	RhB	94.4	Chang et al. (2012)
Bi_2WO_6	MG	87.4	Chen et al. (2012)
(POMs) $(NH_4)_3[PW_{12}O_{40}]$	MG	72	Liu et al. (2016)
Ag/CdS	MG	78	Mandal et al. (2019)
ZnO	MG	93	Saïkia et al. (2015)
Fe_3O_4@mesoporous SBA-15	MG	79	Aliyan et al. (2013)
$MgCr_2O_4$–BiOI NCs	RhB and MG	99.5 and 98.2	Present work

72–92% respectively. Here, MCO-BOI NCs was found to be an effective nanomaterial for the complete mineralization of pollutants such as RhB and MG.

5. Effects of environmental parameters on photodegradation of RhB and MG

The effect of parameters such as NCs concentration, dye concentration and pH on photodegradation was investigated. The photocatalytic degradation of RhB and MG under different pH 5 to 9 is provided Supplementary material Fig. S2a and S3a respectively. The photocatalytic degradation of RhB by MCO-BIO NCs shows that the degradation was effective at pH 5 and for MG the degradation was effective at pH 6. In addition, the complete degradation of the MG was also observed on pH 8 and pH 9. Here, the photolysis of MG takes place under alkaline pH hence complete degradation observed in absence of NCs. Further, the photocatalytic degradation experiment was performed by varying the concentration of NCs and the results conclude that the rate of degradation increased with increase in concentration of NCs (Supplementary material Fig. S2b and S3b). The higher in the concentration of NCs possess higher in the surface area of the NCs which can provide more surface to interact with organic molecules, thus shows the higher the degradation of RhB and MG at higher concentration of NCs. In addition, the similar experiment was performed by varying the concentration of RhB and MG and the results showed that the complete mineralization was observed from 5 to 20 mg/L (Supplementary material Fig. S2 and S3).

The complete mineralization of RhB and MG was determined by total organic carbon (TOC) analysis. TOC in pollutant before and after degradation was estimated by walkey-black method. Here, the results showed that the TOC removal after degradation of RhB and MG was calculated to be 92 and 94%. Thus the results shows that the complete mineralization of RhB and MG under visible light.

6. Radical scavenging, stability and reusability

The reusability of MCO-BIO NCs is essential for the photocatalytic degradation of RhB and MG, and its reusability efficiency was determined by six cycle tests (Supplementary material Fig. S4a1 and b1). The result concludes that the reusability efficiency on the degradation of RhB and MG was calculated to be 100% and 95.2% respectively. The difference in the degradation efficiency of the first and sixth cycle on RhB was found to be negligible (equal to zero) and in the case of MG was 4.6%. The effect of different quencher on the capture of •OH, $\bullet O_2$, h^+ and e^- was determined by the addition of IPA, BQ, EDTA and $AgNO_3$ to the reaction mixture respectively. The quencher factors on the degradation of RhB and MG was illustrated in Supplementary material Fig. S4a2 and b2. The radical quenching experiment concluded that the formation of •OH leads to the effective degradation of RhB and MG. The stability of MCO-BIO NCs was analyzed by performing XRD and FIR after the irradiation of NCs under visible light. XRD pattern of MCO-BIO NCs showed similar peaks position and intensity before and after the irradiation under visible light (Supplementary material Fig. S4c). FTIR spectra after the irradiation of MCO-BIO NCs showed addition peaks at 3592.5 and 1685 cm^{-1}corresponds to the OH group (Supplementary material Fig. S4d) (Finocchio et al., 1995).

7. Parameter optimization

RSM was performed on the photocatalytic degradation of RhB and MG by MCO-BIO NCs and the result was displayed in Supplementary material Fig. S5. RSM plot was performed by varying the parameter (pH, different concentration of NPs and different concentration of NPs) with the response on the degradation of RhB and MG. The result concludes that the surface plot on the degradation of RhB indicate the effective degradation at 8 of pH, 20 mg/L NCs concentration and 15 mg/L of concentration RhB and the degradation was effective at 9 of pH, 20 mg/L NCs concentration and 10 mg/L of concentration MG.

8. Photocatalytic mechanism of MCO-BIO NCs

Fig. 5 shows that the schematic representation of photocatalytic mechanism of MCO-BIO NCs. The VB and CB values of the MCO-BOI NCs were calculated by the empirical equation:

$$E_{CB} = X - E_C - \frac{1}{2}E_g \quad (3)$$

$$E_{VB} = E_{VB} + E_g \quad (4)$$

Where X, E_c and E_g indicates absolute electronegativity, energy of free electrons and band gap energy of the corresponding material respectively. The VB and CB of MCO were determined to be 0.42 eV and 1.98 eV respectively. The VB and CB of BIO were 1.78 eV and 4.20 eV respectively. The electron will be exiting from VB to CB when it is irradiated under visible light. The band gap energy of MCO-BIO NCs (2.16 eV) confirm its visible light excitation efficiency. Here, MCO-BIO NCs follow Z scheme. The PL spectra of MCO-BIO NCs confirm the effective charge separation than the pure MCO and BIO NPs. The EIS and PL results also confirms the effective charge transfer and lower in the rate recombination of MCO-BIO NCs, which enhance the photocatalytic property of nanohybrid. The CB of MCO was less negative than −0.33 eV ($O_2^-/O^{2-\cdot}$ Vs NHE), this shows that the electron does not efficiency to convert $O_2^-$to$\bullet O_2$ radical (Feng et al., 2021). The E_{VB} of BOI was high positive than 2.34 eV ($OH^-/OH^\cdot$ vs NHE), thus hydroxyl ions interact with holes to form $OH^\cdot$ radicals (Feng et al., 2021). Here, the scavenging results also shows that the formation of OH• radical played the major role in photocatalytic reaction (Cao et al., 2017). In addition, the computational analysis by gaussian DFT proves that ΔE_{abs} of $H_2O$was higher than pure MCO-BIO NCs. This causes the increase in the formation of h^+ for the effective formation of OH• from adsorbed O_2 and H_2O for effective photocatalytic degradation of RhB and MG.

9. Photocatalytic degradation pathway of RhB and MG

The photocatalytic degradation of RhB and MG by MCO-BIO NCs was determined by GC-MS and it is illustrated in Supplementary material Fig. 6. DFT was performed for both RhB and MG and the Fukui theorem

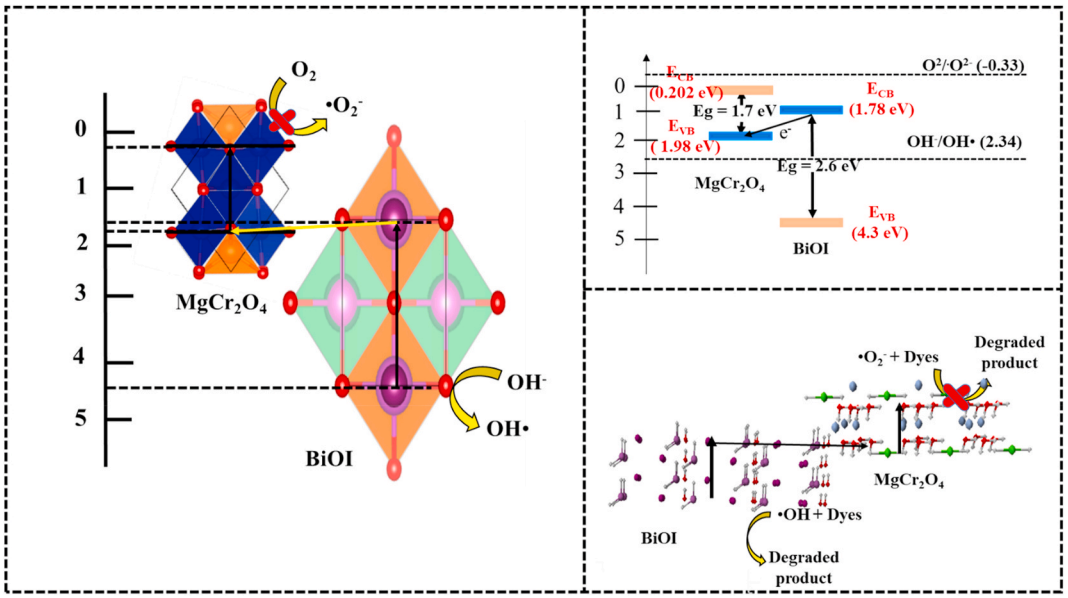

Fig. 5. Photocatalytic mechanism of $MgCr_2O_4$–BiOI NCs.

performed by Material studio (Wang et al., 2020a,b). Here, •OH attacked at N1, C3 and cleaves the organic compound, further oxides for the complete mineralization of RhB. The degradation pathway shows that the radical attack with the formation of intermediate and further oxidize to form CO_2 and H_2O (Supplementary materials Fig. S6a) (Natarajan et al., 2011). In addition, the MG degradation pathway shows that •OH attacked at C6 cleaves the organic compound, further oxides for the complete mineralization of the MG. Here, the degradation pathway shows that the radical attach with the formation of intermediate as and further oxidize to form CO_2 and H_2O (Supplementary materials Fig. S6a) (Diao et al., 2013). TOC results also good agreed with the complete mineralization of RhB and MG by MCO-BOI NCs.

10. Toxicology prediction

The acute and chronic toxicity of the intermediate and degraded product prediction of RhB and MG by MCO-BOI NCs was by ECOSAR program (Wang et al., 2020a,b). The toxicity prediction on the intermediates and degraded product of RhB and MG was illustrated in Supplementary material Fig. S7. Here, RhB and MG show non harmful effect on fish, daphnia and algae. Nevertheless, the photolysis of RhB and MG leads to the formation of intermediate which is toxic and causes hazardous effect on the environmental living organism (Wright et al., 2010; Culp et al., 2006). In addition, the higher the concentration of dye causes the COD (chemical oxygen demand) in the water, which damage in the pond eco system (Culp et al., 2006). Here, photocatalytic degradation of RhB and MG by MCO-BOI NCs shows complete mineralization of the organic pollutant, which was also confirmed by TOC analysis. Thus, the results shows that the complete mineralization of RhB and MG by MCO-BOI NCs did not show any toxic effect on the environmental living organism (Supplementary material Fig. S7).

11. Conclusion

To sum up, the 3D BOI nanoflower modified MCO NCs was synthesized by simple co-precipitation method and it showed enhanced photocatalytic activity against RhB and MG dye. The NCs was successfully characterized by TEM, XRD and XPS. PL and EIS results show that MCO-BOI NCs shows effective charge separation and lower in the rate of recombination than pure MCO and BOI NPs. The photocatalytic activity of NCs against RhB and MG shows complete mineralization of dyes. The scavenging results shows the formation of •OH play a major role in the degradation of RhB and MG. In addition, the prediction of degradation pathway of RhB and MG was performed by Fukui theorem and their toxicology of intermediate was studied by ECOSAR program. The study suggests the practical application of MCO-BOI NCs in environmental remediation for the removal of toxic pollutants.

Credit author statement

S. Balasurya: Methodology, Writing – original draft, Investigation, Formal analysis. **Mohammad K. Okla:** Writing - review & editing, Funding acquisition. **Asmaa Mohebaldin:** Investigation, Formal analysis. **Abdullah A. Al-ghamdi:** Formal analysis, Writing – review & editing. **Mostafa A. Abdel-Maksoud:** Investigation, Formal analysis. **Bander Almuqedhi:** Investigation, Formal analysis. **Hamada AbdElgawad:** Investigation, Formal analysis. **Ajith M. Thomas:** Investigation, Formal analysis. **Lija L. Raju:** Investigation, Formal analysis. **S. Sudheer Khan:** Writing - review & editing, Funding acquisition, Supervision.

Declaration of competing interest

The authors declare that they have no known competing financialinterestsor personal relationships that could have appeared to influence the work reported in this paper.

Acknowledgements

The authors extend their appreciation to the Researchers Supporting Project number (RSP-2021/374) King Saud University, Riyadh, Saudi Arabia. Authors thank the management of Bannari Amman Institute of Technology, Sathyamangalam for providing the necessary facilities to carry out the research work.

Appendix A. Supplementary data

Supplementary data to this article can be found online at https://doi.org/10.1016/j.jenvman.2022.114614.

References

Abbasi, A., Hamadanian, M., Salavati-Niasari, M., Mortazavi-Drazkollah, S., 2017. Facile sizecontrolled preparation of highly photocatalytically active $ZnCr_2O_4$ and $ZnCr_2O_4$/

Ag nanostructures for removal of organic contaminants. J. Colloid Interface Sci. 500, 276–284.
Abbasi, A., Sajadi, S.M.S., Amiri, O., Hamadanian, M., Moayedi, H., Salavati-Niasari, M., Beigi, M.M., 2019. $MgCr_2O_4$ and $MgCr_2O_4$/Ag nanostructures: facile size-controlled synthesis and their photocatalytic performance for destruction of organic contaminants. Compos. B Eng. 175, 107077.
Akhundi, A., Habibi-Yangjeh, A., 2017. Graphitic carbon nitride nanosheets decorated with $CuCr_2O_4$ nanoparticles: novel photocatalysts with high performances in visible light degradation of water pollutants. J. Colloid Interface Sci. 504, 697–710.
Aliyan, H., Fazaeli, R., Jalilian, R., 2013. Fe_3O_4@mesoporous SBA-15: a magnetically recoverable catalyst for photodegradation of malachite green. Appl. Surf. Sci. 276, 147–153.
Al-Qahtani, W.H., Balasurya, S., Okla, M.K., Abdel-maksoud, M.A., AbdElgawad, H., Al-ghamdi, A.A., Thomas, A.M., Raju, L.L., Sudheer Khan, S., 2022. Synthesis and application of CdS nanoparticles-decorated core-shell Ag@Ni nanohybrids for visible-light spectrophotometric assay of sulfide in aqueous sample. Spectrochim. Acta Mol. Biomol. Spectrosc. 270, 120793.
Andrade, M.J., Lima, M.D., Bonadiman, R., Bergmann, C.P., 2006. Nanocrystalline pirochromite spinel through solution combustion synthesis. Mater. Res. Bull. 41, 2070–2079.
Balasurya, S., Syed, A., Swedha, M., Harini, G., Elgorban, A.M., Zaghloul, N.S.S., Das, A., Sudheer Khan, S., 2021a. A novel SPR based Fe@Ag core–shell nanosphere entrapped on starch matrix an optical probe for sensing of mercury(II) ion: a nanomolar detection, wide pH range and real water sample application. Spectrochim. Acta Mol. Biomol. Spectrosc. 263, 120204.
Balasurya, S., Alfarraj, S., Raju, L.L., Chinnathambi, A., Ali Alharbi, S., Thomas, A.M., Sudheer Khan, S., 2021b. Novel $CoWO_4$-Ag_2MoO_4 NCs: synthesis, enhanced photocatalytic activity under visible-light irradiation and its antimicrobial activity. Surface. Interfac. 25, 101237.
Balasurya, S., Okla, M.K., Abdel-maksoud, M.A., Ahamad, S.R., Almasoud, F., AbdElgawad, H., Thomas, A.M., Raju, L.L., Sudheer Khan, S., 2022. Fabrication of Ag-$ZnCo_2O_4$ framework on chitosan matrix for discriminative dual mode detection of S^{2-} ions and cysteine, and cyto-toxicological evaluation. J. Mol. Liq. 347, 118356.
Bergwerff, A.A., Scherpenisse, P., 2003. Determination of residues of malachite green in aquatic animals. J. Chromatogr. B 788, 351–359.
Bessekhouad, Y., Robert, D., Weber, J., 2004. Bi_2S_3/TiO_2 and CdS/TiO_2 heterojunctions as an available configuration for photocatalytic degradation of organic pollutant. J. Photochem. Photobiol. Chem. 163, 569–580.
Cao, W., An, Y., Chen, L., Qi, Z., 2017. Visible-light-driven Ag_2MoO_4/Ag_3PO_4 composites with enhanced photocatalytic activity. J. Alloys Compd. 701, 350–357.
Chang, X., Gondal, M.A., Saadi, A.A.A., Ali, M.A., Shen, H., Zhou, Q., Zhang, J., Du, M., Liu, Y., Ji, G., 2012. Photodegradation of Rhodamine B over unexcited semiconductor compounds of BiOCl and BiOBr. J. Colloid Interface Sci. 377, 291–298.
Chen, C.C., Lu, C.S., Chung, Y.C., Jan, J.L., 2007. UV light induced photodegradation of malachite green on TiO_2 nanoparticles. J. Hazard Mater. 141, 520–528.
Chen, G.Y., Miao, S.I., 2010. HPLC Determination and MS confirmation of malachite green, gentian violet, and their leuco metabolite residues in channel catfish muscle. J. Agric. Food Chem. 58, 7109–7114.
Chen, Y., Zhang, Y., Liu, C., Lu, A., Zhang, W., 2012. Photodegradation of malachite green by nanostructured Bi_2WO_6 visible light-induced photocatalyst. Int. J. Photoenergy 510158.
Culp, S.J., Beland, F.A., Heflich, R.H., Benson, R.W., Blankenship, L.R., Webb, P.J., Mellick, P.W., Trotter, R.W., Shelton, S.D., Greenlees, K.J., Manjanatha, M.G., 2002. Mutagenicity and carcinogenicity in relation to DNA adduct formation in rats fed leucomalachite green. Mutat. Res. Fund Mol. Mech. Mutagen 506 (507), 55–63.
Culp, S.J., Mellick, P.W., Trotter, R.W., Greenlees, K.J., Kodell, R.L., Beland, F.A., 2006. Carcinogenicity of malachite green chloride and leucomalachite green in B6C3F1 mice and F344 rats. Food Chem. Toxicol. 44, 1204–1212.
Di, J., Xia, J., Li, H., Guo, S., Dai, S., 2017. Bismuth oxyhalide layered materials for energy and environmental applications. Nanomater. Energy 41, 172–192.
Di, J., Zhu, C., Ji, M., Duan, M., Long, R., Yan, C., Gu, K., Xiong, J., She, Y., Xia, J., Li, H., Liu, Z., 2018. Defect-rich $Bi_{12}O_{17}Cl_2$ Nanotubes self-Accelerating charge separation for boosting photocatalytic CO_2 reduction. Angewandte Chemie International 57, 14847–14851.
Di, J., Xia, J., Chisholm, M.F., Zhong, J., Chen, C., Cao, X., Dong, F., Chi, Z., Chen, H., Weng, Y.X., Xiong, J., Yang, S.Z., Li, H., Liu, Z., Dai, S., 2019. Defect-Tailoring mediated electron–hole separation in single-unit-cell Bi_3O_4Br nanosheets for boosting photocatalytic hydrogen evolution and nitrogen fixation. Adv. Mater. 31, 1807576.
Di, J., Song, P., Zhu, C., Chen, C., Xiong, J., Duan, M., Long, R., Zhou, W., Xu, M., Kang, L., Lin, B., Liu, D., Chen, S., Liu, C., Li, H., Zhao, Y., Li, S., Yan, Q., Song, L., Liu, Z., 2020. Defect-Tailoring mediated electron–hole separation in single-unit-cell Bi_3O_4Br nanosheets for boosting photocatalytic hydrogen evolution and nitrogen fixation. ACS Mater. Lett. 2, 1025–1032.
Diao, Z., Li, M., Zeng, F., Song, L., Qiu, R., 2013. Degradation pathway of malachite green in a novel dual-tank photoelectrochemical catalytic reactor. J. Hazard Mater. 260, 585–592.
Dong, W.H., Wu, D.D., Luo, J.M., Xing, Q.J., Liu, H., Zou, J.P., Luo, X.B., Min, X.B., Liu, H.L., Luo, S.L., Au, C.T., 2017. Coupling of photodegradation of RhB with photoreduction of CO_2 over rGO/$SrTi_{0.95}Fe_{0.05}O_{3-\delta}$ catalyst: a strategy for one-pot conversion of organic pollutants to methanol and ethanol. J. Catal. 349, 218–225.
Drazic, G., Trontelj, M., 1989. Preparation and properties of ceramic sensor elements based on $MgCr_2O_4$. Sensor. Actuator. B Chem. 18, 407–414.
Fan, Q., Huang, Y., Zhang, C., Liu, J., Piao, L., Yu, Y., Zuo, S., Li, B., 2016. Superior nanoporous graphitic carbon nitride photocatalyst coupled with CdS quantum dots for photodegradation of RhB. Catal. Today 264, 250–256.
Feng, D., He, J., Zheng, L., Jiang, W., Zhang, C., Li, L., Song, J., Yao, W., 2021. Enhanced catalytic performance with Fe@α-Fe_2O_3 thin nanosheets by synergistic effect of photocatalysis and Fenton-like process. J. Phys. Chem. Solid. 150, 109886.
Finocchio, E., Busca, G., Lorenzelli, V., Willey, R.J., 1995. The activation of hydrocarbon CH bonds over transition metal oxide catalysts: a FTIR study of hydrocarbon catalytic combustion over $MgCr_2O_4$. J. Catal. 151, 204–215.
Finocchio, E., Ramis, G., Busca, G., Lorenzelli, V., Willey, R.J., 1996. On the mechanisms of light alkane catalytic oxidation and oxy-dehydrogenation: an FT-IR study of the nbutane conversion over $MgCr_2O_4$ and a Mg-vanadate catalyst. Catal. Today 28, 381–389.
Fischer, A.R., Werner, P., Goss, K.U., 2011. Photodegradation of malachite green and malachite green carbinol under irradiation with different wavelength ranges. Chemosphere 82, 210–214.
Guo, J.F., Ma, B., Yin, A., Fan, K., Dai, W.L., 2011. Photodegradation of rhodamine B and 4-chlorophenol using plasmonic photocatalyst of Ag-AgI/Fe_3O_4@ SiO_2 magnetic nanoparticle under visible light irradiation. Appl. Catal., B 101, 580–586.
He, H., Xue, S., Wu, Z., Yu, C., 2016. Synthesis and characterization of robust Ag_2S/Ag_2WO_4 composite microrods with enhanced photocatalytic performance. J. Mater. Res. 17, 2598–2607.
Kim, T.Y., Lee, D.H., Shim, Y.C., Bu, J.U., Kim, S.T., 1992. Effects of alkaline oxide additives on the microstructure and humidity sensitivity of $MgCr_2O_4$-TiO_2. Sensor. Actuator. B Chem. 9, 221–225.
Kim, B.N., Hiraga, K., Morita, K., Sakka, Y., 2001. A high-strain-rate superplastic ceramic. Nature 413, 288.
Li, H., Cao, X., Zhang, C., Yu, Q., Zhao, Z., Niu, X., Sun, X., Liu, Y., Ma, L.I., Li, Z., 2017. Enhanced adsorptive removal of anionic and cationic dyes from single or mixed dye solutions using MOF PCN-222. RSC Adv. 7, 16273–16281.
Lin, Z., Li, J., Zheng, Z., Yan, J., Liu, P., Wang, C., Yang, G.W., 2015. Electronic reconstruction of α-Ag_2WO_4 nanorods for visible-light photocatalysis. ACS Nano 9, 7256–7265.
Liu, F., Chung, S., Oh, G., Seo, T.S., 2012. Three-dimensional graphene oxide nanostructure for fast and efficient water-soluble dye removal. ACS Appl. Mater. Interfaces 4, 922–927.
Liu, C.G., Zheng, T., Liu, S., Zhang, H.Y., 2016. Photodegradation of malachite green dye catalyzed by Keggin-type polyoxometalates under visible-light irradiation: transition metal substituted effects. J. Mol. Struct. 1110, 44–52.
Malato, S., Fernandez-Ibanez, P., Maldonado, M.I., Blanco, J., Gernjak, W., 2009. Decontamination and disinfection of water by solar photocatalysis: recent overview and trends. Catal. Today 147, 1–59.
Mandal, R.K., Purkayastha, M.D., Majumder, T.P., 2019. Silver modified cadmium oxide – a novel material for enhanced photodegradation of malachite green. Optik 180, 174–182.
Martinho, H., Moreno, N.O., Sanjurjo, J.A., Rettori, C., García-Adeva, A.J., Huber, D.L., Oseroff, S.B., Ratcliff, W., Cheong, S.W., Pagliuso, P.G., Sarrao, J.L., Martins, G.B., 2001. Magnetic properties of the frustrated antiferromagnetic spinel $ZnCr_2O_4$ and the spin-glass $Zn_{(1-x)}Cd_xCr_2O_{4(x¼0.05,0.10)}$. Phys. Rev. B 64, 024408.
Mittelstaedt, R.A., Mei, N., Webb, P.J., Shaddock, J.G., Dobrovolsky, V.N., McGarrity, L. J., Morris, S.M., Chen, T., Beland, F.A., Greenlees, K.J., Heflich, R.H., 2004. Genotoxicity of malachite green and leucomalachite green in female Big Blue B_6C_3F (1) mice. Mutat. Res. Genet. Toxicol. Environ. Mutagen 561, 127–138.
Natarajan, K., Natarajan, T.S., Bajaj, H.C., Tayade, R.J., 2011. Photocatalytic reactor based on UV-LED/TiO_2 coated quartz tube for degradation of dyes. Chem. Eng. J. 178, 40–49.
Natarajan, T.S., Thomas, M., Natarajan, K., Bajaj, H.C., Tayade, R.J., 2011. Study on UV-LED/TiO_2 process for degradation of Rhodamine B dye. Chem. Eng. J. 169, 126–134.
Nayak, H., Bhatta, D., 2002. Catalytic effects of magnesium chromite spinel on the decomposition of lanthanum oxalate. Thermochim. Acta 389, 109–119.
Ochiai, T., Fujishima, A., 2012. Photoelectrochemical properties of TiO_2 photocatalyst and its applications for environmental purification. J. Photochem. Photobiol. C Photochem. Rev. 13, 247–262.
Parasuraman, D., Serpe, M.J., 2011. Poly (n-isopropylacrylamide) microgels for organic dye removal from water. ACS Appl. Mater. Interfaces 3, 2732–2737.
Phan, T.T.N., Nikoloski, A.N., Bahri, P.A., Li, D., 2018. Heterogeneous photo-Fenton degradation of organics using highly efficient Cu-doped $LaFeO_3$ under visible light. J. Ind. Eng. Chem. 61, 53–64.
Pingale, S.S., Patil, S.F., Vinod, M.P., Pathak, G., Vijayamohanan, K., 1996. Mechanism of humidity sensing of Ti-doped $MgCr_2O_4$ ceramics. Mater. Chem. Phys. 46, 72–76.
Pirhashemi, M., Habibi-Yangjeh, A., Pouran, S.R., 2018. Review on the criteria anticipated for the fabrication of highly efficient ZnO-based visible-light-driven photocatalysts. J. Ind. Eng. Chem. 62, 1–25.
Rajamohan, S., Kumaravel, V., Muthuramalingam, R., Ayyadurai, S., Wahab, A.A., Wak, B.S.K., Kang, M., Sreekantan, S., 2017. Fe_3O_4-Ag_2WO_4: facile synthesis, characterization and visible light assisted photocatalytic activity. New J. Chem. 41, 11722–11730.
Raza, A., Qin, Z., Ahmad, S.O., Ikram, A.M., Li, G., 2021. Recent advances in structural tailoring of BiOX-based 2D composites for solar energy harvesting. J. Environ. Chem. Eng. 9, 106569.
Saikia, L., Bhuyan, D., Saikia, M., Malakar, B., Dutta, D.K., Sengupt, P., 2015. Photocatalytic performance of ZnO nanomaterials for self sensitized degradation of malachite green dye under solar light. Appl. Catal. Gen. 490, 42–49.
Srivastava, S., Sinha, R., Roy, D., 2004. Toxicological effects of malachite green. Aquat. Toxicol. (N. Y.) 66, 319–329.

Szilágyi, I.M., Fórizs, B., Rosseler, O., Szegedi, Á., Németh, P., Király, P., Tárkányi, G., Vajna, B., Varga-Josepovits, K., László, K., Tóth, A.L., Baranyai, P., Leskeläc, M., 2012. WO_3 photocatalysts: influence of structure and composition. J. Catal. 294, 119–127.

Wang, K.S., Lin, C.L., Wei, M.C., Liang, H.H., Li, H.C., Chang, C.H., Fang, Y.T., Chang, S. H., 2010. Effects of dissolved oxygen on dye removal by zero-valent iron. J. Hazard Mater. 182, 886–895.

Wang, K., Xu, J., Hua, X., Li, N., Chen, M., Teng, F., Zhu, Y., Yao, W., 2014. Highly efficient photodegradation of RhB–MO mixture dye wastewater by Ag_3PO_4 dodecahedrons under acidic condition. J. Mol. Catal. Chem. 393, 302–308.

Wang, R., Liu, G., Chu Lau, T., 2015. Rational design of Ag@Ag-Bi-$KBa_2Ta_5O_{15}$ nanocomposites as efficient plasmonic photocatalysts for degradation of organic pollutants in water under visible light. Appl. Catal. Gen. 496, 17–24.

Wang, J., Gao, B., Dou, M., Huang, X., Ma, Z., 2020a. A porous g-C_3N_4 nanosheets containing nitrogen defects for enhanced photocatalytic removal meropenem: mechanism, degradation pathway and DFT calculation. Environ. Res. 184, 109339.

Wang, J., Shen, M., Wang, H., Du, Y., Zhou, X., Liao, Z., Wang, H., Chen, Z., 2020b. Red mud modified sludge biochar for the activation of peroxymonosulfate: singlet oxygen dominated mechanism and toxicity prediction. Sci. Total Environ. 740, 140388.

Wen, X.J., Niu, C.G., Zhang, L., Zeng, G.M., 2017. Fabrication of SnO_2 nanopaticles/BiOI n–p heterostructure for wider spectrum visible-light photocatalytic degradation of antibiotic oxytetracycline hydrochloride. ACS Sustain. Chem. Eng. 5, 5134–5147.

Wright, G.D., 2010. Antibiotic resistance in the environment: a link to the clinic? Curr. Opin. Microbiol. 13, 589–594.

Xia, Z., Shi, B., Zhu, W., Lü, C., 2021. Temperature-responsive polymer-tethered Zr-porphyrin MOFs encapsulated carbon dot nanohybrids with boosted visible-light photodegradation for organic contaminants in water. Chem. Eng. J. 426, 131794.

Zhang, Y., Lin, C., Lin, Q., Jin, Y., Wang, Y., Zhang, Z., Lin, H., Long, J., Wang, X., 2018. CuI-BiOI/Cu film for enhanced photo-induced charge separation and visible-light antibacterial activity. Appl. Catal., B 235, 238–245.

Zhang, Y., An, Y., Liu, C., Wang, Y., Song, Z., Li, Y., Meng, W., Qi, F., Xu, B., Croue, J.P., Yuan, D., Ikhlaq, A., 2019. Catalytic ozonation of emerging pollutant and reduction of toxic by-products in secondary effluent matrix and effluent organic matter reaction activity. Water Res. 166, 115026.